

Validation and uncertainty analysis of global luminescent oil-film skin-friction field measurement

Taekjin Lee¹, Taku Nonomura^{1,3}, Keisuke Asai¹
and Jonathan W Naughton²

¹ Department of Aerospace Engineering, Tohoku University, Aoba-Ku, Sendai, Miyagi 980-8579, Japan

² Department of Mechanical Engineering, University of Wyoming, Laramie, Wyoming 82071, United States of America

E-mail: lee.taekjin@aero.mech.tohoku.ac.jp

Received 14 August 2019, revised 15 October 2019

Accepted for publication 25 October 2019

Published 31 December 2019



Abstract

Results from a skin-friction-field measurement method using global luminescent oil-film images, in which the oil film covers a large portion of the surface, were examined by comparing them with those obtained from conventional hot-wire measurements. The measurement processes including calibrations, oil-film image acquisition, and image processing are explained, and error sources are analyzed. The experimental results show that the skin frictions measured by both methods in a turbulent boundary layer on a flat surface agree when the oil-film thickness is less than the height of the viscous sublayer (corresponding to an oil-film thickness of less than five wall units). The uncertainty of the measurements is presented. When the measurement conditions were optimum (illumination, exposure time, frame rate, oil height, etc), the uncertainty was approximately 3%–4%.

Keywords: skin friction, wall shear stress, image-based measurement, oil film, uncertainty analysis

(Some figures may appear in colour only in the online journal)

1. Introduction

Knowledge of the skin-friction field, also called the surface shear stress field, on the surface of objects is one of important requirements of fluid dynamics. Measuring the skin-friction distribution helps characterize the state of a boundary layer, the overall viscous drag, the flow topology including flow separation and attachment, and the heat flux distribution. However, skin friction is one of the most difficult quantities to measure on the surface [1–4]. Liquid crystal coating methods [5], elastic polymer films [6], near-wall particle image velocimetry (PIV) [7], and quantitative evaluation of mini-tuft behavior [8] have all been used for the measurement of skin-friction distributions. However, these methods require special surface treatment and/or have limitations on the geometry or the accuracy.

Oil-film techniques, which have the advantage of flexible adaption to various surfaces, measure the temporal and spatial evolution of an oil film, solve the governing equation of the thin oil film, and then calculate the skin friction [9]. Oil-film interferometry (OFI), invented by Tanner and Blows [10], was first implemented as a point-based measurement and subsequently extended to an image-based global measurement by Monson *et al* [11], Naughton and Brown [12], Zilliac [13], and Garrison and Ackman [14]. Liu and Sullivan [15] suggested an alternative method for measuring oil film using luminescent intensity, which was extended to a global measurement by Liu *et al* [16] and is called the global luminescent oil-film (GLOF) technique. Global approaches require additional information to determine the skin-friction vector field from an oil-film thickness scalar field. Most OFI techniques assume the flow direction is known or measured separately. For example, Mosharov *et al* [17] put particles in the oil film and used cross-correlation analysis to determine skin-friction

³ Also at JST, PRESTO, Aoba-Ku, Sendai, Miyagi 980-8579, Japan.

directions. Liu *et al* [16] adopted GLOF utilizing a modified variation-based optical flow method to solve the thin oil-film equation, but the approach requires an arbitrary parameter on which its result substantially depends. Kurita and Iijima [18] combined GLOF and local OFI methods, and Husen *et al* [19] used a molecular flow tagging technique that writes a pattern within the oil film. Lee *et al* [20] proposed a novel approach for GLOF image analysis—a linear least-squares (LLS) method solving the thin oil-film equation, which does not require arbitrary parameters.

This paper demonstrates an evaluation of the GLOF measurement technique based on the LLS method and clarifies the requirements necessary for the technique to be implemented successfully. First, the theoretical background of the GLOF method, oil-film data processing, and uncertainty propagation equation are explained. Second, the technique is evaluated through a wind tunnel test using a flat plate turbulent boundary layer, and the results are compared with those determined from hot-wire measurements. In addition, an uncertainty analysis with an element-wise survey is demonstrated, and the contributions of each error source are clarified. Finally, proper measurement conditions for obtaining feasible results are presented.

2. Working principal

2.1. Governing equation of thin oil film

The behavior of an oil film on a surface can be described by the thin oil-film equation [9],

$$\frac{\partial h}{\partial t} + \nabla \cdot \left(\frac{h^2}{2\mu} \boldsymbol{\tau} - \frac{h^3}{3\mu} (\nabla p - \rho \mathbf{a}) \right) = 0, \quad (1)$$

where h is the oil-film thickness, μ is the dynamic viscosity of oil, $\boldsymbol{\tau}$ is the skin friction, p is the pressure, ρ is the density, and \mathbf{a} is the body acceleration. The pressure includes the effect of the surface tension, $p = p_a + \sigma_o/R_o$, where p_a is the air pressure, σ_o is the surface tension of the oil, and R_o is the radius of the curvature of the oil-film surface. The pressure gradient and body acceleration terms are negligible when the skin-friction term is comparatively large. The parameter ε_{PC} indicates the ratio of the Poiseuille flow term to the Couette flow term

$$\varepsilon_{PC} = \frac{2}{3} \frac{h \|\nabla C_p - \rho \mathbf{a}/q_\infty\|}{\|C_f\|}, \quad (2)$$

where $q_\infty = 0.5\rho_a u_0^2$ is the dynamic pressure, ρ_a is the air density, u_0 is the free-stream velocity, C_p is the pressure coefficient, and C_f is the skin-friction coefficient. For $\varepsilon_{PC} \ll 1$, equation (1) becomes

$$\frac{\partial h}{\partial t} + \nabla \cdot \left(\frac{h^2}{2\mu} \boldsymbol{\tau} \right) = 0. \quad (3)$$

2.2. Measuring oil-film thickness from luminescent intensity

The oil-film thickness h is measured from image data using [21]

$$h = h_* \frac{I}{I_{\text{ref}}} = h_* r, \quad (4)$$

where I is the intensity of the luminescent oil-film image, I_{ref} is the intensity of the excitation light image, r is the ratio of the intensities (the so-called ‘ratioed image’ that eliminates the effect of non-uniform illumination), and h_* is the constant of proportionality relating the value r to the oil-film thickness h , i.e. the unit thickness of the intensity ratio.

The parameter h_* is measured by the integral method [19, 21] using an image of an oil droplet of known volume on the test surface. If the volume of the oil droplet v_{droplet} is known, an average thickness \bar{h} can be measured in the image. Therefore,

$$h_* = \frac{\bar{h}}{r_{\text{cal}}} = \frac{v_{\text{droplet}}/S}{\bar{r}_{\text{cal}}} = \frac{v_{\text{droplet}}}{n_{\text{cal}} \bar{r}_{\text{cal}} x_*^2}, \quad (5)$$

where $\bar{\phi}$ indicates the ensemble average of an arbitrary quantity ϕ , \bar{r}_{cal} is the ensemble-averaged ratioed image of the droplet, S is the corresponding area, n_{cal} is the total pixel number of the area, and x_* is the unit length of the spatial resolution on the measurement surface.

2.3. Determination of skin-friction field from oil-film images

When τ is assumed to be a temporal constant, the optimum skin-friction field $\hat{\boldsymbol{\tau}}$ that most likely satisfies equation (3) for the given data is determined [20] as

$$\hat{\boldsymbol{\tau}} = \arg \min_{\boldsymbol{\tau} \in \mathbb{R}^N} \sum_k \|\mathbf{e}_k(\boldsymbol{\tau})\|_2^2, \quad (6)$$

where $\|\cdot\|_2^2$ means the squared Euclidean norm, k is the moment index which is between the image pair, and \mathbf{e}_k is the residual vector at k th image pair data, which is defined as

$$\mathbf{e}_{m,k} = \left\{ \nabla \cdot \left(\frac{h_{n,k}^2}{2\mu} \boldsymbol{\tau}_n \right) \right\}_m + \left. \frac{\partial h}{\partial t} \right|_{m,k}, \quad (7)$$

where m is the node index, n is the $\boldsymbol{\tau}$ vector index, and N is the dimension of the $\boldsymbol{\tau}$ vector. Note that the image pairs and the skin-friction field are considered to be vectorized, i.e. matrices are converted into column vectors.

For numerically processing the oil-film data, a two-dimensional staggered grid in Cartesian coordinates is defined as shown in figure 1, where i and j indicate the grid coordinate, the square indicates e is at the node, the circle indicates h at the center of the cell, and the arrow indicates $\boldsymbol{\tau}$ at the face of the cell. The residual vector $\mathbf{e}_k \in \mathbb{R}^M$ is

$$\mathbf{e}_k(\boldsymbol{\tau}) = \frac{h_*^2}{\mu x_*} \mathbf{A}_k \boldsymbol{\tau} - \frac{h_*}{t_*} \mathbf{b}_k, \quad (8)$$

where

$$\mathbf{A}_k = \frac{1}{2} \boldsymbol{\Delta}_x \{ \text{diag}(\mathbf{M}_{c2f} \mathbf{r}_k) \}^2, \quad (9)$$

$$\mathbf{b}_k = -\boldsymbol{\Delta}_t \mathbf{M}_{c2n} \mathbf{r}_k, \{ \text{diag}(\mathbf{M}_{c2f} \mathbf{r}_k) \}^2, \quad (10)$$

$$\boldsymbol{\tau} = [\tau_1 \quad \tau_2 \quad \cdots \quad \tau_n \quad \cdots \quad \tau_N]^T, \{ \text{diag}(\mathbf{M}_{c2f} \mathbf{r}_k) \}^2, \quad (11)$$

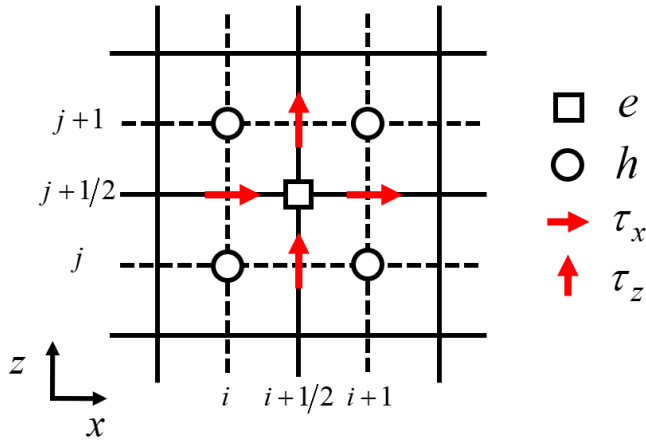


Figure 1. Two-dimensional staggered grid for oil-film data processing. i, j : grid coordinate index; square: residual; circle: oil-film data; arrow: skin-friction vector.

$$\mathbf{r}_k = [r_1 \ r_2 \ \cdots \ r_p \ \cdots \ r_p]^T, \quad (12)$$

t_* is the time interval of the image pair, ‘diag’ indicates the diagonal matrix operator, superscript T indicates the transposed matrix, $\boldsymbol{\tau}$ is the vectorized skin-friction field, \mathbf{r}_k is the vectorized ratioed image pair at the moment k , $\Delta_x \in \mathcal{R}^{M \times N}$ is the spatial difference scheme matrix, $\Delta_t \in \mathcal{R}^{M \times 2M}$ is the temporal difference scheme matrix, $\mathbf{M}_{c2f} \in \mathcal{R}^{N \times P}$ is the cell-to-face interpolation matrix, $\mathbf{M}_{c2n} \in \mathcal{R}^{2M \times P}$ is the cell-to-node interpolation matrix, n is the vector field index, N is the dimension of the vector field, p is the image vector index, P is the dimension of the image vector, and M is the total number of the nodes. The solution of equation (6) is [20, 22]

$$\hat{\boldsymbol{\tau}} = \frac{\mu x_*}{t_* h_*} \mathbf{C}^{-1} \mathbf{d} = \tau_* \hat{\boldsymbol{\tau}}, \quad (13)$$

where

$$\begin{aligned} \mathbf{C} &= \sum_k \mathbf{A}_k^T \mathbf{A}_k \\ &= \frac{1}{4} \sum_k \{ \text{diag}(\mathbf{M}_{c2f} \mathbf{r}_k) \}^2 \Delta_x^T \Delta_x \{ \text{diag}(\mathbf{M}_{c2f} \mathbf{r}_k) \}^2, \end{aligned} \quad (14)$$

$$\mathbf{d} = \sum_k \mathbf{A}_k^T \mathbf{b}_k = -\frac{1}{2} \sum_k \{ \text{diag}(\mathbf{M}_{c2f} \mathbf{r}_k) \}^2 \Delta_x^T \Delta_t \mathbf{r}_k, \quad (15)$$

$$\tau_* = \frac{\mu x_*}{t_* h_*} = \frac{\mu x_*^3 n_{\text{cal}} \bar{r}_{\text{cal}}}{t_* v_{\text{droplet}}}, \quad (16)$$

τ_* is the unit skin friction, $\hat{\boldsymbol{\tau}} = \mathbf{C}^{-1} \mathbf{d}$ is the estimated normalized skin-friction vector, and \sim indicates variables that are based on the image units such as the pixels and the frame interval.

For the simplest case, where only one node and 2×2 pixels exist on each image pair, the scheme matrices and vectors are

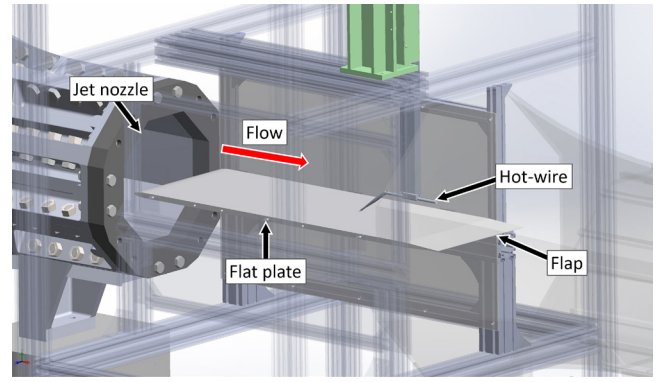


Figure 2. Flat plate installed in an open-jet test section of the wind tunnel.

$$\begin{aligned} \Delta_x &= \begin{bmatrix} -1 \\ 1 \\ -1 \\ 1 \end{bmatrix}^T, \quad \Delta_t = \begin{bmatrix} -1 \\ 1 \end{bmatrix}^T, \\ \mathbf{M}_{c2f} &= \frac{1}{4} \begin{bmatrix} 1 & 0 & 1 & 0 & 1 & 0 & 1 & 0 \\ 0 & 1 & 0 & 1 & 0 & 1 & 0 & 1 \\ 1 & 1 & 0 & 0 & 1 & 1 & 0 & 0 \\ 0 & 0 & 1 & 1 & 0 & 0 & 1 & 1 \end{bmatrix}, \\ \mathbf{M}_{c2n} &= \frac{1}{4} \begin{bmatrix} 1 & 1 & 1 & 1 & 0 & 0 & 0 & 0 \\ 0 & 0 & 0 & 0 & 1 & 1 & 1 & 1 \end{bmatrix}, \end{aligned} \quad (17)$$

$$\mathbf{r}_k = \begin{bmatrix} r_{i-1/2, j-1/2, k-1/2} \\ r_{i+1/2, j-1/2, k-1/2} \\ r_{i-1/2, j+1/2, k-1/2} \\ r_{i+1/2, j+1/2, k-1/2} \\ r_{i-1/2, j-1/2, k+1/2} \\ r_{i+1/2, j-1/2, k+1/2} \\ r_{i-1/2, j+1/2, k+1/2} \\ r_{i+1/2, j+1/2, k+1/2} \end{bmatrix},$$

$$\boldsymbol{\tau} = [\tau_{i, j+1/2} \quad \tau_{i+1, j+1/2} \quad \tau_{i+1/2, j} \quad \tau_{i+1/2, j+1}]^T,$$

where the spatial and temporal partial derivatives are approximated to second-order accuracy.

2.4. Uncertainty propagation

The uncertainty of the estimated skin friction is derived from equations (13) and (16) based on an uncertainty propagation analysis [23]. When the correlation between the uncertainty of the individual measurement is negligible, the total uncertainty is

$$U_{\hat{\boldsymbol{\tau}}} \simeq |\hat{\boldsymbol{\tau}}| \left(\frac{U_{\mu}^2}{\mu^2} + 3^2 \frac{U_{x_*}^2}{x_*^2} + \frac{U_{t_*}^2}{t_*^2} + \frac{U_{v_{\text{droplet}}}^2}{v_{\text{droplet}}^2} + \frac{U_{\bar{r}_{\text{cal}}}^2}{\bar{r}_{\text{cal}}^2} + \frac{U_{\hat{\boldsymbol{\tau}}}^2}{\hat{\boldsymbol{\tau}}^2} \right)^{0.5}, \quad (18)$$

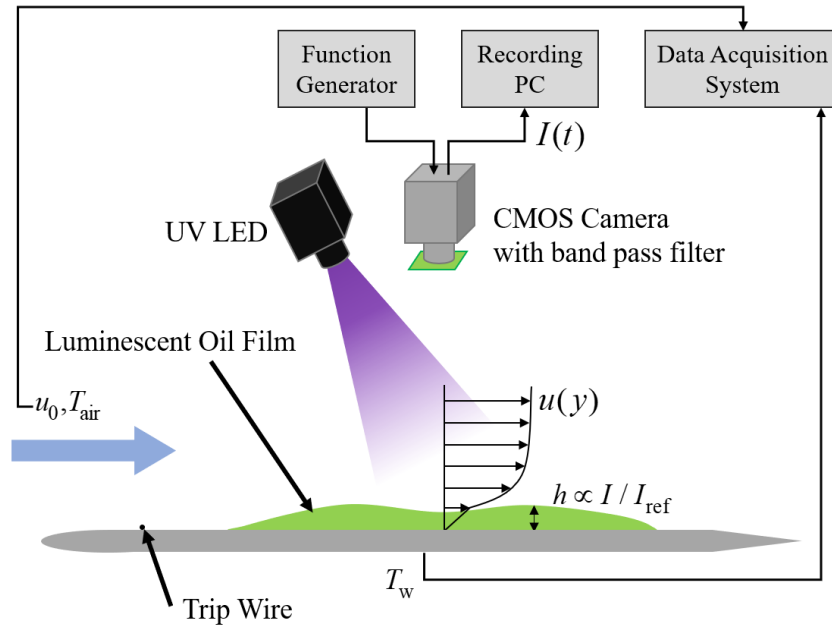


Figure 3. Schematic diagram of GLOF measurement system. Oil-film distribution is measured by an optical system which is composed of a CMOS camera system, an optical band pass filter, and an excitation light source. Flow conditions were recorded by a data acquisition system.

where U_i denotes the uncertainty of variable i . Because x_* is used for the calibration of h_* , the sensitivity of x_* is relatively higher than the others. The uncertainty of the normalized skin friction $U_{\hat{\tau}}$ is caused by image noise, and, therefore,

$$U_{\hat{\tau}} = sU_r, \quad (19)$$

where s is the sensitivity coefficient of the image error propagation in the numerical process, defined as

$$s^2 \equiv \frac{U_{\hat{\tau}}^2}{U_r^2} = \sum_{p,k} \left(\frac{\partial \hat{\tau}}{\partial r_{p,k}} \right)^2. \quad (20)$$

The sensitivity s can be obtained by two approaches: the analytical method and the Monte Carlo method. The analytical derivation of s is shown in the appendix. The Monte Carlo method measures s in a statistical approach, adding normally distributed random errors $\epsilon = \mathcal{N}(0, \sigma_\epsilon^2)$ for the given ratioed images and sampling the standard deviation of $\hat{\tau}$.

3. Experiment

3.1. Wind tunnel and test surface

The skin friction on the surface beneath a turbulent boundary layer on a flat plate was measured using both GLOF and hot-wire anemometer techniques. The small low-turbulence wind tunnel in the Institute of Fluid Science, Tohoku University, was employed for the experiment. The flat plate model with side walls was installed in the open-jet test section, in which the jet nozzle has an octagonal cross-section (figure 2). The plate model made of aluminum has a thickness of 12 mm, a width of 290 mm, a length of 897 mm including a 100 mm flap, and a 6:1 elliptical leading edge. A 0.81 mm diameter

trip wire was set at 50 mm from the leading edge to trip the boundary layer.

3.2. Measurement system

The experimental measurement system is shown in figure 3. The luminescent oil was made by dissolving luminescent dye (1-Chloro-9,10-bis(phenylethynyl)anthracene, 1-Cl-BPEA) into dimethyl silicone oil (DM-FLUID-350cs, from Shin-Etsu Silicone) of a 7ppm weight ratio. The bottle containing the mixture was put in an ultrasonic cleaner, and vibration was applied for 1 h ensuring the dye was dissolved in the oil. The resulting luminescent oil is clear green, absorbs ultraviolet (UV) to blue light (peak of 472 nm), and emits green light (peak of 493, 528 nm) [24]. The oil film is applied on the aluminum surface without any treatment. For the excitation light source, a UV light-emitting diode unit (IL-106, from HARDsoft), which has a peak wavelength of 395 nm, was used. A 16-bit monochrome CMOS camera (C13440, from Hamamatsu Photonics) was used for sequential GLOF image acquisition, and an optical bandpass filter (470–550 nm, from Asahi-Spectra) separated the excitation light from the luminescent light. The camera was set to the external trigger mode, and a function generator (WF1974, from NF Corporation) controlled the frame rate. A data acquisition system records the flow data and the plate temperature.

3.3. Boundary layer measurement

The boundary layer characteristics and the reference skin-friction values were obtained using velocity profiles obtained using hot-wire measurements. The mean velocity profiles

Table 1. Flow and boundary layer conditions on the free-stream velocity of 20, 30, 40, 50, and 60 m s⁻¹. δ_v : the viscous sublayer thickness where $y^+ = 5$.

u_0 (m s ⁻¹)	Re_x (10 ⁶)	Re_θ (10 ³)	δ (mm)	δ_v (μ m)	τ_{ref} (Pa)	C_f (10 ⁻³)
20	0.548	1.43	9.29	88.5	0.918	3.84
30	0.825	2.01	8.72	62.3	1.881	3.52
40	1.091	2.63	8.45	48.6	3.098	3.27
50	1.361	3.23	8.43	39.7	4.621	3.11
60	1.636	3.85	8.33	34.1	6.376	3.01

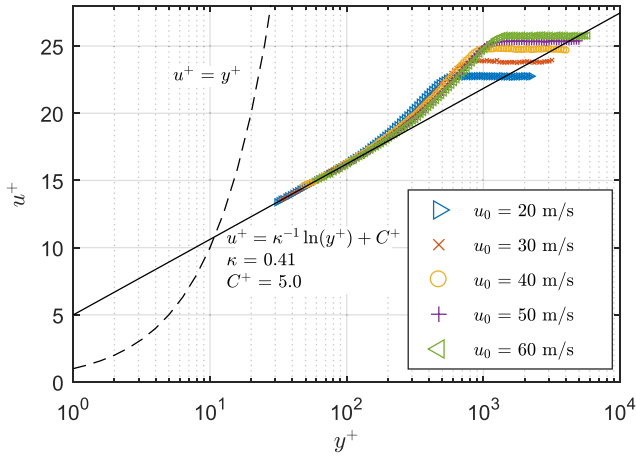


Figure 4. Mean velocity profile of boundary layers in wall coordinates.

were measured using a constant-temperature anemometer (model 1010, from KANOMAX) together with a single wire probe (0251R-T5, from KANOMAX), at a reference position 430 mm from the leading edge and 145 mm from the side wall. The measurement was conducted without oil film. The hot wire was calibrated against a pitot tube installed in the wind tunnel based on

$$E^2 = (T_{hw} - T_0)(Au^n + B), \quad (21)$$

where E is the hot-wire bridge voltage, T_{hw} is the hot-wire temperature, T_0 is the flow temperature, and u is the flow velocity. The constants A , B , and n were determined from a least-squares fit. The mean velocity profile of the turbulent boundary layer follows the law of the wall [25–27],

$$u^+ = \begin{cases} y^+, & \text{for } y^+ < 5 \\ \kappa^{-1} \ln(y^+) + C^+, & \text{for } 30 < y^+ \end{cases} \quad (22)$$

where $u^+ = u/u_\tau$ is the dimensionless velocity, $u_\tau = (\tau/\rho_{air})^{0.5}$ is the friction velocity, $y^+ = yu_\tau/\nu_{air}$ is the normalized distance from the wall, $\kappa = 0.41$ is the von Kármán constant, and $C^+ = 5.0$ is a constant. The skin friction was determined by the Clauser chart method [28], in which the error is expected to be approximately 2.5% [29]. The fitting data were selected in the range of $y^+ < 100$ in the case of $u_0 = 20$ m s⁻¹, $y^+ < 120$ in the case of $u_0 = 30$ m s⁻¹, and $y^+ < 150$ for the other cases. The viscous sublayer thickness $\delta_v = 5\nu_{air}/u_\tau$ is defined for further analysis.

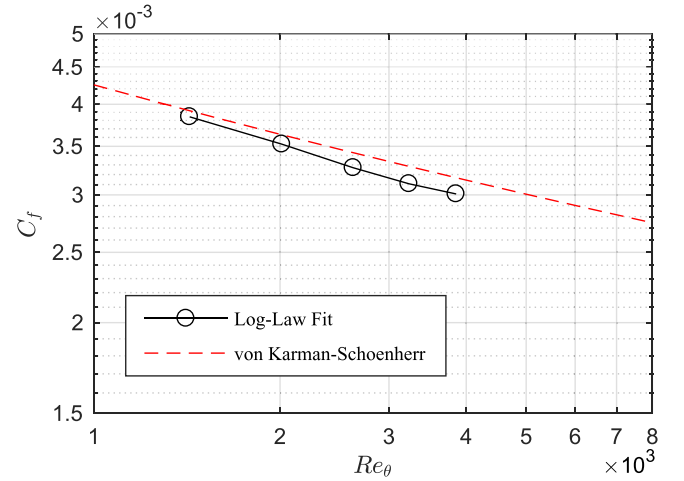


Figure 5. Skin-friction coefficient variation with a momentum-thickness Reynolds number.

3.4. Flow and measurement conditions

The wind tunnel tests were conducted at free-stream velocities of 20, 30, 40, 50, and 60 m s⁻¹. The flow conditions are shown in table 1, and the corresponding velocity profiles are shown in figure 4. The measured skin-friction coefficient with the momentum-thickness Reynolds number Re_θ was compared with the von Kármán–Schoenherr equation [30],

$$(1/C_f) = 17.08 (\log_{10} Re_\theta)^2 + 25.11 \log_{10} Re_\theta + 6.012, \quad (23)$$

as shown in figure 5. The correlation between C_f and Re_θ provides evidence that the boundary layer studied here is typical. The deviation of the theoretical value to the measured value is 2.6% in the lowest Re_θ case; the deviations have become larger along with the increase of Re_θ . The reason can be considered to be that the velocity at low y^+ is limited in the higher Re_θ cases, and therefore the measurement error increased.

The GLOF measurement conditions are shown in table 2. The frame rates, the power of the excitation lights, and the exposure time are selected for each condition so that the oil film can be appropriately measured. The parameter ε_{PC} was evaluated in the given flow conditions. The pressure gradient was in the order of 10 Pa m⁻¹ and the plate was leveled; the reference h was considered as in the order of δ_v . At the lowest C_f condition, $\varepsilon_{PC} \simeq 0.05\%$, confirming that equation (3) is valid. Before the images are processed, they are down-sampled, and each pixel interval is set to be five times larger than the viscous sublayer thickness. In table 2, the group refers to the group of tests in which the calibration procedure described in the next section 3.5 is performed.

3.5. Calibration procedure

The calibration parameters are measured using the following procedures. The oil viscosity μ is calculated using values provided by the manufacturer and the measured temperature. The kinetic viscosity $\nu = \mu/\rho$ and the density ρ of the silicone oil can be calculated by the following equations [31],

Table 2. Measurement and data processing conditions.

	u_0 (m s ⁻¹)	T_{oil} (K)	μ (Pa s)	Scale (%)	x_* (mm)	t_* (s)	t_{exp} (ms)	Light (a.u.)	h_* (μ m)
Group 1	20	297.0	0.345	36.57	0.443	1/20	30	8	182.9
	30	297.1	0.344	52.02	0.311	1/20	30	8	182.9
	40	297.3	0.343	66.61	0.243	1/20	30	8	182.9
Group 2	20	298.5	0.336	36.62	0.443	1/8	35	18	121.2
	30	297.5	0.341	52.08	0.311	1/8	70	18	60.6
	40	299.0	0.332	66.70	0.243	1/8	70	18	60.6
	50	299.7	0.329	81.68	0.198	1/8	70	18	60.6
	60	299.5	0.329	95.19	0.170	1/8	70	18	60.6
Group 3	30	298.7	0.335	52.02	0.311	1/8	35	18	121.9
	40	299.1	0.332	66.62	0.243	1/8	35	18	121.9
	50	299.9	0.327	81.58	0.198	1/8	35	18	121.9
	60	299.8	0.328	95.08	0.170	1/8	35	18	121.9

$$\log_{10} \nu = 763.1 \text{ K} \cdot (1/T - 1/T_0) + \log_{10} \nu_0, \quad (24)$$

$$\rho = 965 \text{ kg m}^{-3} - 0.860 \text{ kg m}^{-3} \text{ K}^{-1} \cdot (T - T_0), \quad (25)$$

where $T_0 = 298 \text{ K}$ is the standard oil temperature, and $\nu_0 = 350 \times 10^{-6} \text{ m}^2 \text{ s}^{-1}$ is the kinetic viscosity at T_0 . The oil temperature is considered to be the same as the flat plate temperature T_w [3, 32, 33], which is measured during the test. The unit length x_* was measured based on a calibration image of a scale on the test surface, shown in figure 6(a). Two points are taken in the scale image, and the corresponding physical length was read. The unit time t_* corresponds to the image time interval set on the function generator.

The excitation light distribution image I_{exc} is shown in figure 6(b). A high-brightness paper, which generally includes fluorescent dye, was set on the test surface to simulate an even distribution of luminescent oil film, which is hard to achieve with oil present on the surface. However, the intensity is much brighter than that of oil, and therefore, the exposure settings, such as exposure time, were quite different. A Gaussian filter was applied to the excitation image, and small structures such as those caused by paper fibers and uneven fluorescent dye were removed. The oil droplet image I_{cal} was taken to be used with the integral method [21], which obtains h_* from an image of a known volume oil, as shown in figure 6(c). A micro pipette (Biomaster 4830, from Eppendorf) was used, which is suitable for accurately pipetting viscous liquids to apply $10 \mu\text{l}$ oil droplets to the test surface. Figure 6(d) is the background image, an image when there is no oil film on the surface. The observed features are mainly due to the leakage of the excitation light source that has passed through the band pass filter, and, therefore, the scratches on the plate are visible. In this study, the background image was not subtracted from images of the oil, and the effects of this will be discussed later.

3.6. Oil-film distribution measurement and data reduction

The ratioed image is obtained using

$$r = \frac{I}{I_{ref}} = \frac{I_{run} - \overline{I_{dark}}}{I_{exc} - \overline{I_{dark}}}, \quad (26)$$

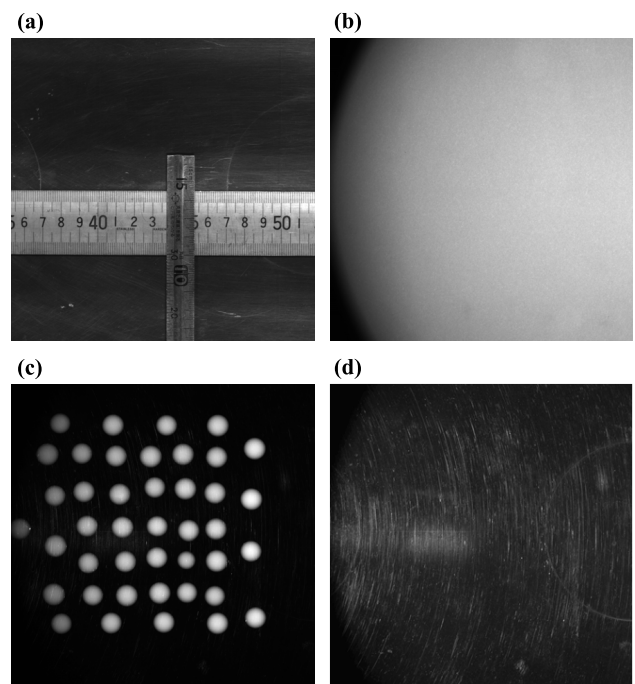


Figure 6. Calibration images: (a) scale on the measuring surface, (b) excitation light distribution, (c) oil droplets, and (d) background (emphasized).

where I_{run} is the oil-film image during measurements, I_{dark} is the dark current image, and I_{exc} is the excitation light distribution image. The unit oil-film thickness h_* of each droplet in the droplet image I_{cal} was calculated using equation (5), and the median value was used. The calibration images I_{dark} , I_{exc} , and $I_{droplet}$ were taken 10 times each and the average images were used.

The data were analyzed using a MATLAB® code [34], where the algorithm is based on the work by Lee *et al* [20]. 200 sequential pairs of GLOF images were used for the data reduction. The region of interest was set to be a square centered on the reference point with a width of 4δ . The sensitivity s was obtained using the Monte Carlo method. Arbitrary noise $\sigma_\epsilon = 0.001$ was added to the given image set. The analysis of 200 pairs of images was repeated 50 times to determine

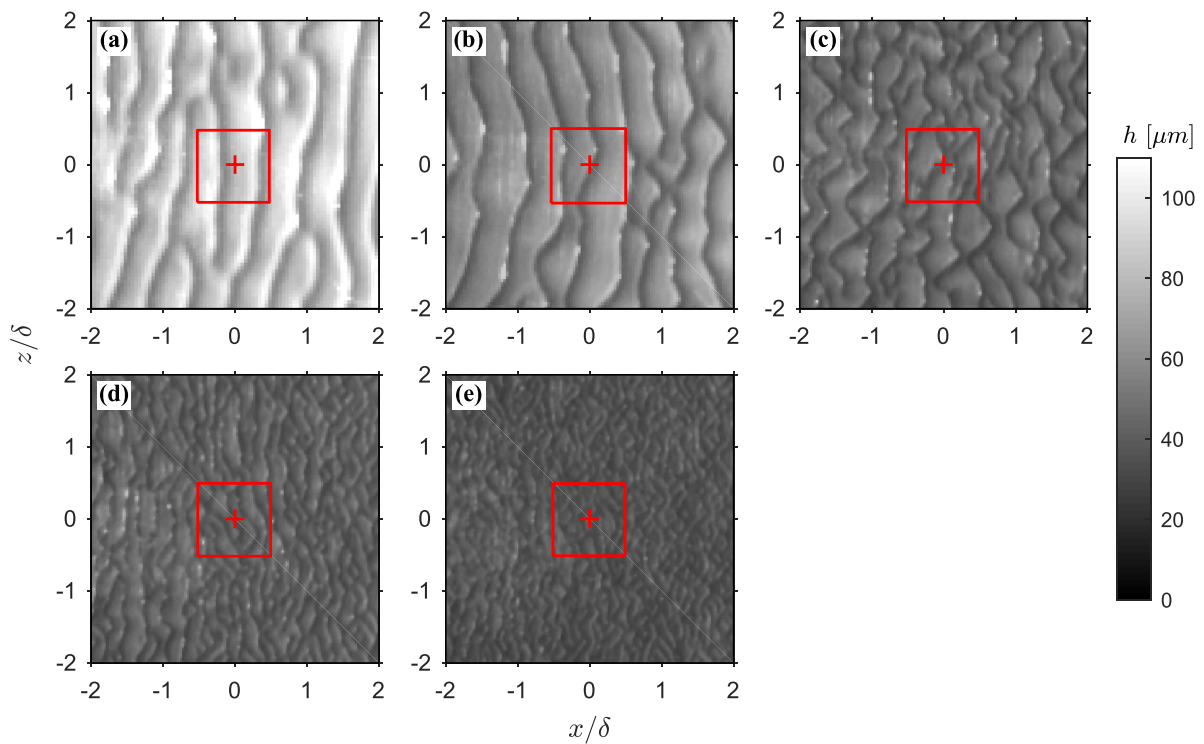


Figure 7. Representative oil-film distributions: (a) $u_0 = 20 \text{ m s}^{-1}$, (b) $u_0 = 30 \text{ m s}^{-1}$, (c) $u_0 = 40 \text{ m s}^{-1}$, (d) $u_0 = 50 \text{ m s}^{-1}$, and (e) $u_0 = 60 \text{ m s}^{-1}$. Red cross: the reference point. Red square: the averaging area for representative values.

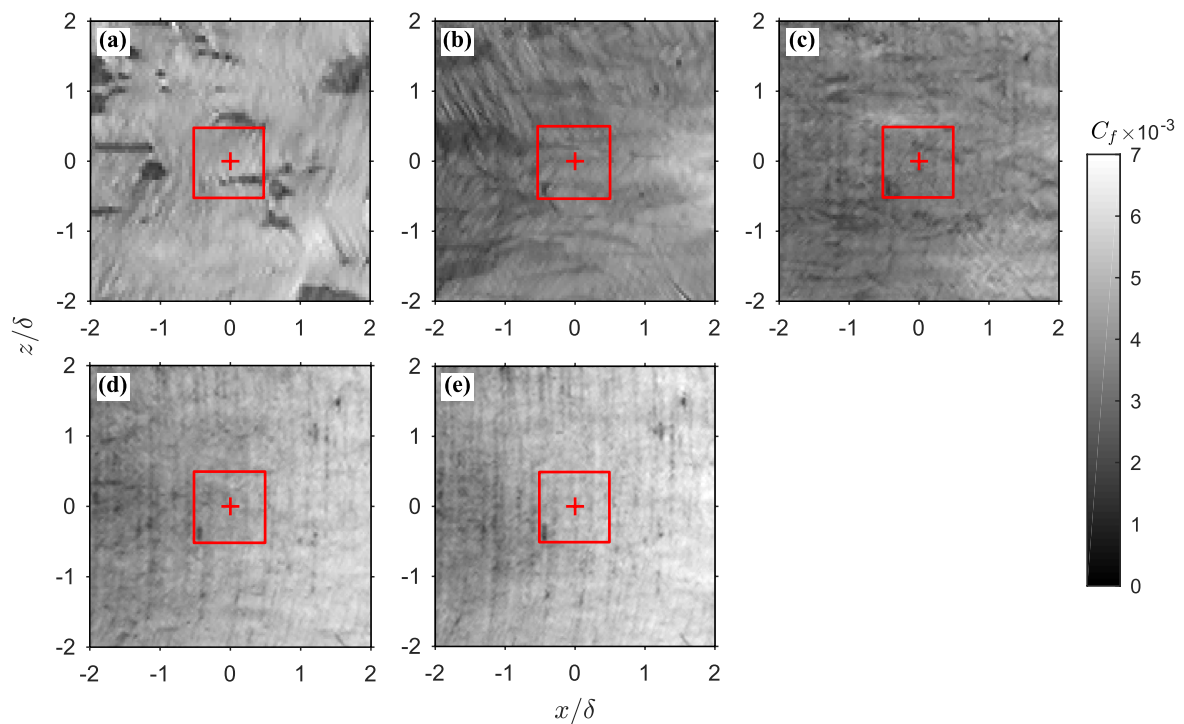


Figure 8. Representative skin-friction coefficient distributions: (a) $u_0 = 20 \text{ m s}^{-1}$, (b) $u_0 = 30 \text{ m s}^{-1}$, (c) $u_0 = 40 \text{ m s}^{-1}$, (d) $u_0 = 50 \text{ m s}^{-1}$, and (e) $u_0 = 60 \text{ m s}^{-1}$. Red cross: the reference point. Red square: the averaging area for representative values.

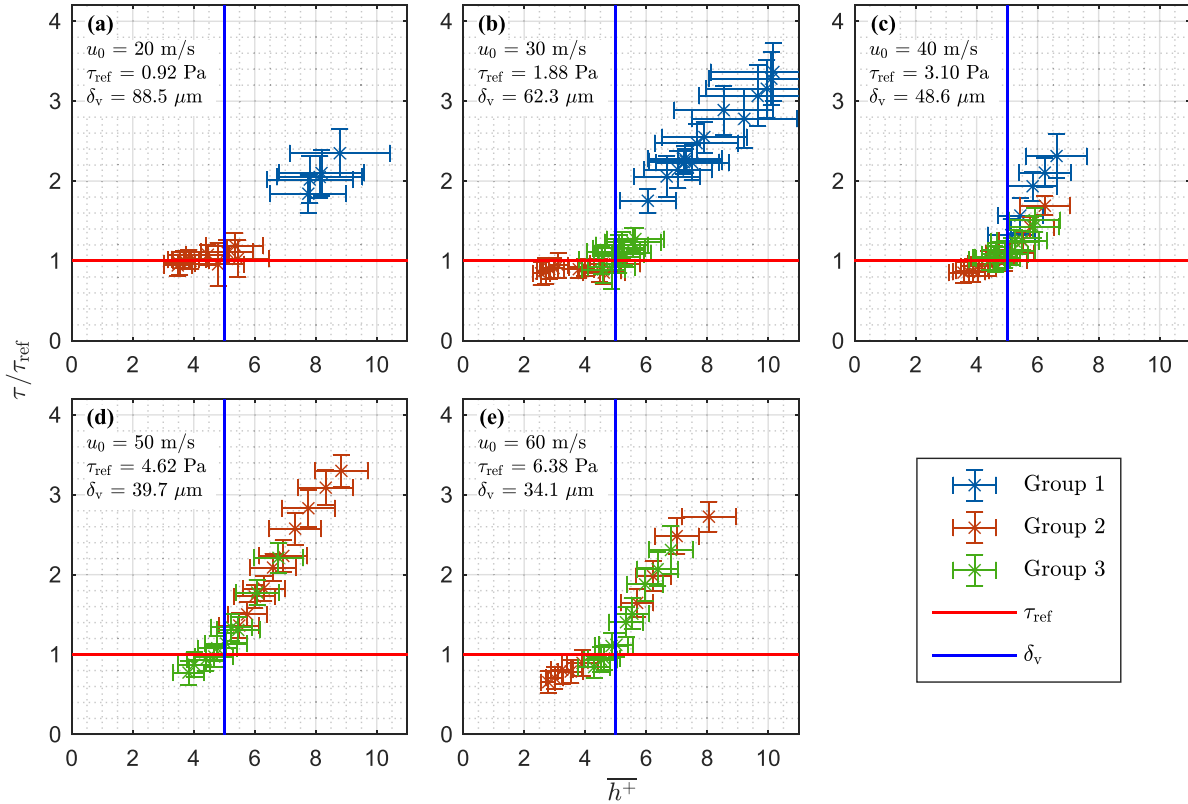


Figure 9. Measured skin friction against average oil-film thickness: (a) $u_0 = 20 \text{ m s}^{-1}$, (b) $u_0 = 30 \text{ m s}^{-1}$, (c) $u_0 = 40 \text{ m s}^{-1}$, (d) $u_0 = 50 \text{ m s}^{-1}$, and (e) $u_0 = 60 \text{ m s}^{-1}$. Red line: the reference skin friction measured by the Clauser chart method. Blue line: the viscous sublayer thickness. Vertical error bar: spatial standard deviation. Horizontal error bar: temporal standard deviation of oil-film thickness, averaged on the averaging area.

the deviation of $\hat{\tau}$, and then the sensitivity was obtained as $s = \sigma(\hat{\tau})/\sigma_\epsilon$. The sensitivities from both the analytical method and the Monte Carlo method showed good agreement when σ_ϵ was smaller than 0.005.

To assess the quality of the estimated skin friction τ , the coefficient of determination is evaluated. The coefficient is given by

$$\mathbf{R}^2 = 1 - \left\{ \sum_k (\mathbf{A}_k \hat{\tau} - \mathbf{b}_k)^{\circ 2} \right\} \oslash \left\{ \sum_k (\mathbf{b}_k - \bar{\mathbf{b}})^{\circ 2} \right\}, \quad (27)$$

where \circ and \oslash are the Hadamard product and division, respectively, R^2 indicates how well the present formulation works, and $\hat{\tau}$ represents the given skin friction. If all data are fully represented by the LLS regression, this value is one. By contrast, a smaller R^2 indicates a poorer regression.

4. Experimental results

The representative oil-film distributions for each flow condition are shown in figure 7, and the corresponding skin-friction distributions are shown in figure 8. Since the present analysis yields the distribution, an averaging area was set to be a square region centered on the reference point with a width of δ , and the parameters determined from the average taken in these areas will be discussed. The cases presented are chosen

such that the average oil-film thickness is closest to the viscous sublayer thickness δ_v . The representative oil-film distributions in figure 7 show that the oil film displays large width waves when u_0 is low. In the $u_0 = 20 \text{ m s}^{-1}$ case, some low C_f spots are present. The low C_f locations observed are caused by debris on the oil film. This effect is stronger when the flow velocity is low. In such a case, a clean surface and dust-free flow will be required to reduce this error. In the higher u_0 cases, a vertical pattern is evident in the C_f distributions, which is similar to the background image shown in figure 6(d). The oil-film thickness can be explained to be overestimated due to the background light, so that the obtained skin-friction field is underestimated. This effect becomes larger when the oil-film image has low intensities.

The values of the skin friction and the average oil-film thickness \bar{h} for each condition are shown in figure 9, and R^2 and the relative uncertainty of the estimated skin friction $U_{\hat{\tau}}/\hat{\tau}$ are shown in figure 10. The results show that the GLOF measurements collapse well with the reference skin-friction value only when \bar{h} is less than the viscous sublayer thickness δ_v . The value of R^2 in $\bar{h} > \delta_v$ is approximately 0.8 in the cases of $u_0 = 20, 30, 40 \text{ m s}^{-1}$, which explains that the increase in $\hat{\tau}$ with increasing \bar{h} is due to the response of the oil film to the flow field, not the image measurement and the numerical process. The model surface becomes hydraulically rough when $\bar{h} > \delta_v$, so the skin friction becomes larger as would be expected, but not desired. In the cases of $u_0 = 50, 60 \text{ m s}^{-1}$,

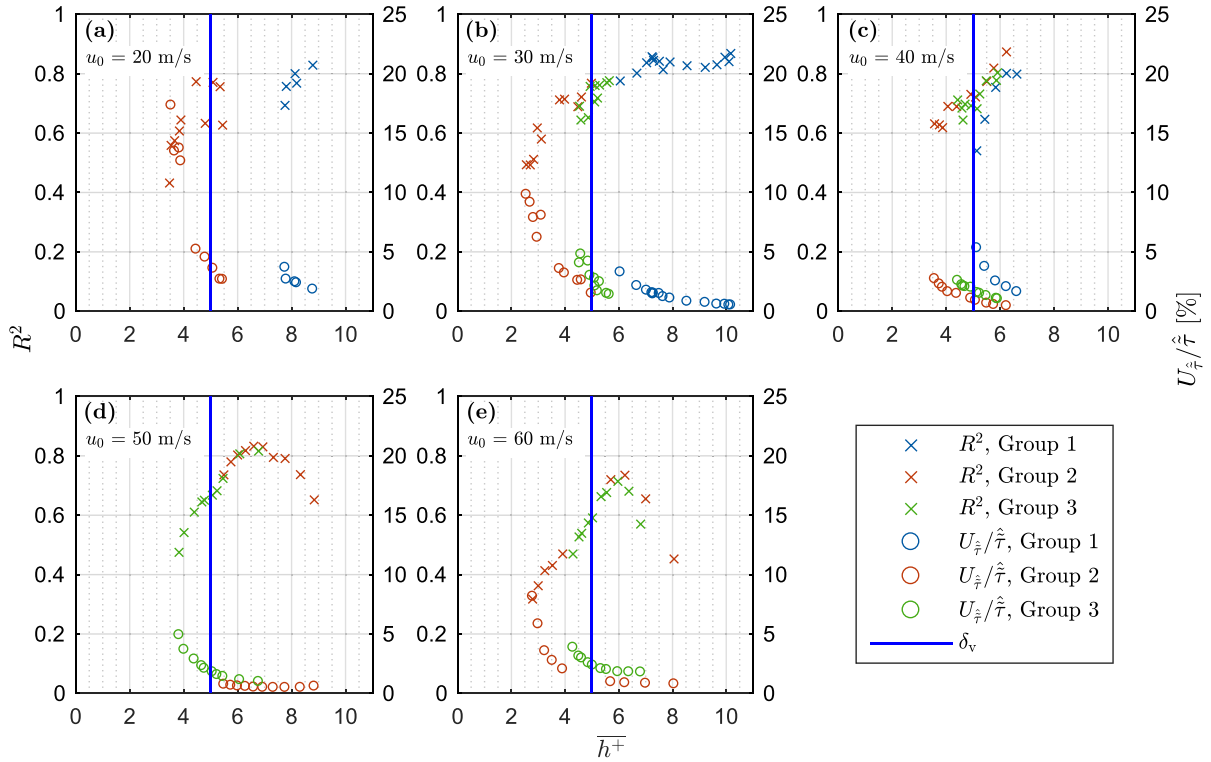


Figure 10. Coefficient of determination R^2 and relative uncertainty of $\hat{\tau}$ against average oil-film thickness \bar{h} : (a) $u_0 = 20 \text{ m s}^{-1}$, (b) $u_0 = 30 \text{ m s}^{-1}$, (c) $u_0 = 40 \text{ m s}^{-1}$, (d) $u_0 = 50 \text{ m s}^{-1}$, and (e) $u_0 = 60 \text{ m s}^{-1}$. Blue line: the viscous sublayer thickness.

R^2 has a peak value near $\bar{h}/\delta_v = 1.3$. The higher \bar{h} cases may exhibit high oil velocity, which violates the optical flow criteria of the measurable maximum velocity [35]. On the other hand, smaller values of \bar{h} yield a smaller R^2 and a higher $U_{\hat{z}}/\hat{\tau}$, indicating that the lower \bar{h} exhibits poorer regressions. For each group, $U_{\hat{z}}/\hat{\tau}$ varies at $\bar{h}/\delta_v = 1$ in the case of $u_0 = 40 \text{ m s}^{-1}$. The higher the unit thickness h_* becomes, the higher $U_{\hat{z}}/\hat{\tau}$ is, which indicates that the same image noise induces the larger h error.

The oil-film thickness in the wall units h^+ can be estimated based on the measured skin-friction value $\hat{\tau}$,

$$\widehat{h^+} = h \frac{(\hat{\tau}/\rho_{\text{air}})^{0.5}}{\nu_{\text{air}}}, \quad (28)$$

where $\widehat{h^+}$ is the oil-film thickness in the estimated wall units. (Figure 11) shows the average h in the wall units against the average \widehat{h} in the estimated wall units. The presented data show that $\widehat{h^+}$ agree well with $\widehat{h^+}$ at $\widehat{h^+} < 5$, and $\widehat{h^+}$ monotonically increases with increasing $\widehat{h^+}$ at $\widehat{h^+} > 5$, therefore, the criteria $\bar{h} < \delta_v$ can be replaced by $\widehat{h^+} < 5$, which indicates that the criteria of the hydraulically smooth surface can be found from the estimated results without additional measurement.

5. Uncertainty analysis

5.1. Elemental error sources

The GLOF measurement consists of various measurements. The uncertainty of each measurement is evaluated, and then

the total uncertainty of the skin friction is considered. With reference to Naughton and Brown's study [36], all significant error sources are listed in table 3 and are categorized by their type (systematic or random) and process (calibration, data acquisition, or data reduction). Calibration processes are for establishing the relationship between measurable variables and desired variables, i.e. from spatio-temporal image data to oil-film dynamics. Data acquisition is the process of measuring the measurable variables. Data reduction processes determine the desired variable τ from the measured variables based on a physical model and assumptions. Among these error sources, only the measurements that could be quantitatively evaluated were selected for performing an uncertainty analysis. Table 3 indicates whether the measurement is included in the analysis or not.

5.2. Oil dynamic viscosity

The oil dynamic viscosity has high sensitivity to its temperature. The sensitivity coefficient around T_0 is calculated from equations (24) and (25) as

$$\left. \frac{\partial \mu}{\partial T} \right|_{T=T_0} = \rho_0 \left. \frac{\partial \nu}{\partial T} \right|_{T=T_0} + \nu_0 \left. \frac{\partial \rho}{\partial T} \right|_{T=T_0} \simeq -6.98 \text{ m Pa s K}^{-1}, \quad (29)$$

and therefore, the uncertainty of the oil viscosity is

$$U_\mu \simeq 6.98 \text{ m Pa s K}^{-1} \cdot U_T. \quad (30)$$

The temperature was measured using a thermocouple (VT3, from CHINO) under the plate model. The sensor tolerance

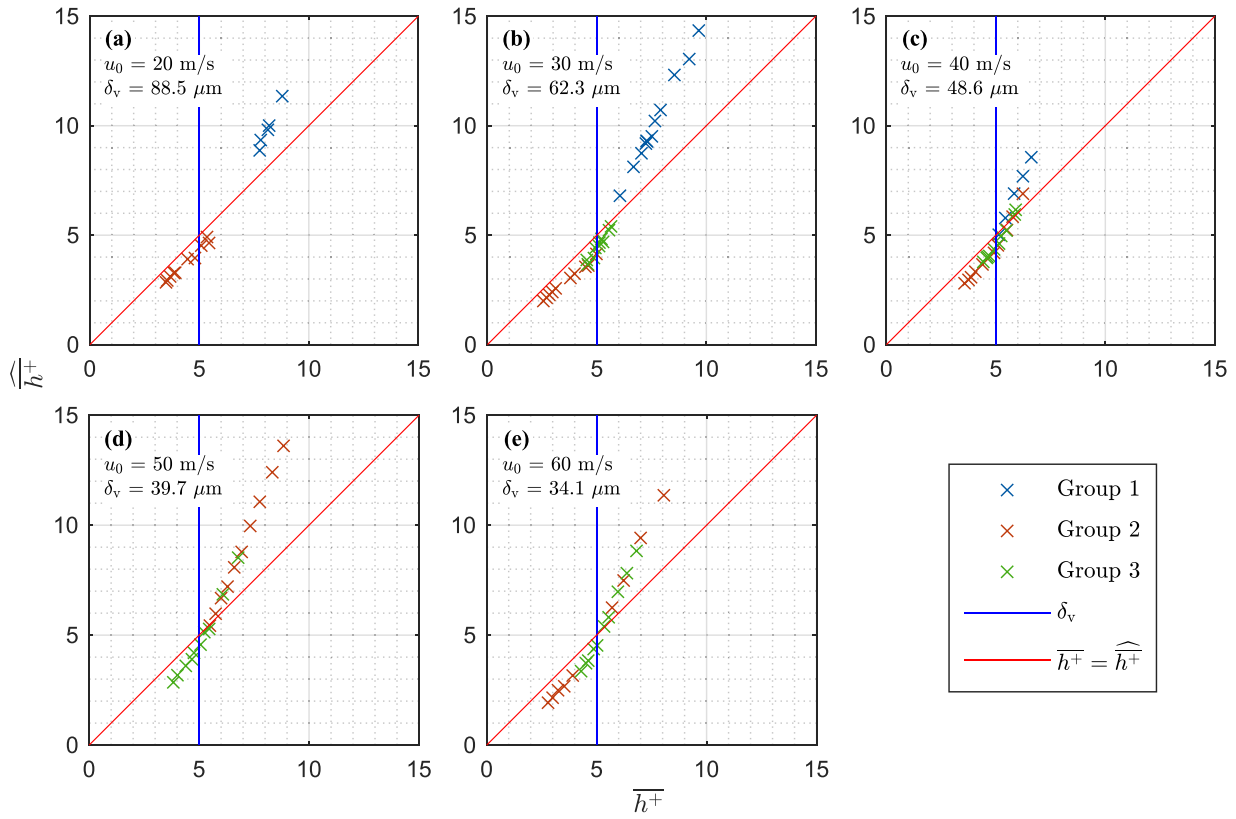


Figure 11. Average oil-film thickness in wall units $\overline{h^+}$ against average oil-film thickness in estimated wall units $\widehat{h^+}$: (a) $u_0 = 20 \text{ m s}^{-1}$, (b) $u_0 = 30 \text{ m s}^{-1}$, (c) $u_0 = 40 \text{ m s}^{-1}$, (d) $u_0 = 50 \text{ m s}^{-1}$, and (e) $u_0 = 60 \text{ m s}^{-1}$. Red line: line of equality. Blue line: the viscous sublayer thickness.

difference was $\pm 1 \text{ K}$ according to the data sheet, which corresponded to a deviation of 1.1 K with a mercury thermometer. When the temperature uncertainty U_T is regarded as 1.1 K , the uncertainty of the oil viscosity U_μ is $7.7 \times 10^{-3} \text{ Pa s}$. The relative uncertainty U_μ/μ is typically 2.3% .

5.3. Unit length

The uncertainty of the unit length x_* is related to camera pixel intervals, the geometry of the surface and the camera angle, the lens distortion, and the calibration process. In this experimental case, the model surface is flat, the camera angle is vertical to the surface, and the lens distortion is negligible. Therefore, x_* is considered to be a constant over the measurement region. In this analysis, only the camera sensor intervals and the scale image calibration were considered. The scale image reading was from 987 pixels to 988 pixels, and the deviation in multiple measurements was approximately 2 pixels. Therefore, the relative uncertainty U_{x_*}/x_* is 0.20% .

5.4. Unit time

The error sources for the unit time are the camera and the function generator accuracy. The camera has a timing jitter of $9.74 \text{ }\mu\text{s}$ [37], and the function generator has a frequency accuracy of $\pm(3 \text{ ppm of setting} + 2 \text{ pHz})$ [38]. Therefore the total uncertainty of time interval U_{t_*} is $9.74 \text{ }\mu\text{s}$ and $9.75 \text{ }\mu\text{s}$

for group 1 and groups 2 and 3, respectively, and the relative uncertainty U_{t_*}/t_* is 0.019% and 0.008% for group 1 and groups 2 and 3, respectively.

5.5. Unit oil-film thickness

The uncertainty of the unit oil-film thickness consists of three sources: the spatial calibration, the oil droplet volume, and the calibration image. The spatial calibration corresponds to x_* , the oil droplet volume uncertainty $U_{v_{\text{droplet}}}$ is caused by pipetting, and the calibration image uncertainty $U_{\overline{r_{\text{cal}}}}$ corresponds to the image uncertainty U_r . A bench test was conducted measuring the weight of $10 \text{ }\mu\text{l}$ oil drops 40 times, and $U_{v_{\text{droplet}}}$ was evaluated. The value was divided by the oil density $9.68 \times 10^2 \text{ kg m}^{-3}$ at the temperature of $21 \text{ }^\circ\text{C}$. The histogram of the oil droplet volume v_{droplet} is shown in figure 12. The result shows that the average of v_{droplet} was $9.81 \text{ }\mu\text{l}$, the average without outliers was $9.85 \text{ }\mu\text{l}$, the standard deviation without outliers was $9.16 \times 10^{-2} \text{ }\mu\text{l}$, and the median was $9.83 \text{ }\mu\text{l}$. The deviation from the target to the median was $1.65 \times 10^{-1} \text{ }\mu\text{l}$. In the calibration process, multiple droplets were measured, and the median value was used. Therefore, the relative uncertainty $U_{v_{\text{droplet}}}/v_{\text{droplet}}$ was 1.65% . The result fits into the micro pipette data sheet values, $\pm 3.0\%$ of the systematic error and $\leq 1.5\%$ of the random error [39]. On the other hand, the uncertainty of the average calibration image $U_{\overline{r_{\text{cal}}}}$ is

Table 3. List of measurement error source. Error types are categorized as follows: S, systematic; R, random; C, calibration; DA, data acquisition; and DR, data reduction. Whether the element is included in the uncertainty analysis is indicated.

Error source	Type	Variable	Description	Included?
Oil				
Kinetic viscosity	S-C	ν	Calibrated by temperature	Yes
Density	S-C	ρ	Calibrated by temperature	Yes
Temperature	R-DA	T_w	Measured on the model	Yes
Geometry				
Curved surface	S-C	x_*	Can be ignored in flat plate	No
Camera angle	S-C	x_*	Depends on viewing angle	No
Excitation light source				
Intensity stability	R-DA	I	Depends on light source	No
Measured by camera				
reflection from model	S-C	I	Depends on surface shape, angles	No
reflection on oil surface	S-DA	I	Depends on instant oil shape	No
Non-uniform illumination				
distribution	S-C	I_{ref}	Calibrated by the reference image	Yes
excitation light refraction	R-DA	I	Lens effect of instant oil shape	No
Camera				
Digitization error	R-DA	I	Depends on dynamic range	Yes
Spatial resolution	S-C	x_*	Camera sensor interval	Yes
Optical distortion	S-C	x_*	Depends on camera lens	No
Electric noise	R-DA	I	Depends on measurement condition	Yes
Frame rate	R-DA	t_*	Depends on camera, timing device	Yes
Calibration procedure				
Oil droplet volume	R-C	v_{droplet}	Accuracy of pipetting	Yes
Reading scale on image	R-C	x_*	Reading scale on the scale image	Yes
Flow field				
Pressure gradient, body forces	S-DR	$\nabla p, \rho \mathbf{a}$	Can be ignored when $\varepsilon_{\text{PC}} \ll 1$	No
Surface tension	R-DR	$\nabla(\sigma_o/R_o)$	Depends on oil-film shape	No
Unsteady flow	R-DR	$\hat{\tau}$	Time constant oil-film model	No
Surface roughness	S-DR	$\hat{\tau}$	If oil-film surface affects the flow	No
Data reduction				
Derivative approximations	S-DR	$\partial/\partial x, \partial/\partial t$	resolution of image data	No
Image down-sampling	S-DR	I	Method-dependent	Yes
Analytical method	S-DR	$\hat{\tau}$	Method, data-dependent	Yes
Thin oil-film modeling	S-DR	$\hat{\tau}$	Assumption of thin layer	No

$$U_{\bar{r}_{\text{cal}}}^2 \simeq \frac{1}{n_{\text{cal}}} U_r^2, \quad (31)$$

where n_{cal} is the total pixel number of the droplet image. The ratioed image uncertainty U_r will be shown in the next subsection. As a result, the relative uncertainty $U_{\bar{r}_{\text{cal}}}/\bar{r}_{\text{cal}}$ was 0.002%–0.003%.

5.6. Normalized skin friction

The uncertainty of the normalized skin friction can be estimated by two parts: the sensitivity s and the ratioed image uncertainty U_r . The sensitivity s was obtained from the Monte Carlo method. The ratioed image uncertainty U_r was obtained from the standard deviation of r in 1000 images taken when $u_0 = 0 \text{ m s}^{-1}$. The exposure time, the frame rate, the excitation light intensity, and the downscaling factor were set to be the same as those in each analysis case. As a result, a U_r of 0.0029 was obtained in most cases. In the cases of group 1

and $u_0 = 20 \text{ m s}^{-1}$ in group 2, steady oil-film images were not taken. Based on the assumption that the image error is not that sensitive to the measurement conditions, a $U_r = 0.0029$ was substituted for the missing cases. The relative uncertainty of $\hat{\tau}$ varies with u_0 . The relationship between $U_{\hat{\tau}}$ and the given image data presented in the previous study [20] explains that the image noise, the image pair number, and the image characteristics determine $U_{\hat{\tau}}$. The characteristics of the given data depend on several factors such as the oil-film thickness and the flow in the real world, as shown in figure 7.

5.7. Total uncertainty

Table 4 shows the measurement uncertainties and the total uncertainty for each measurement condition for those cases in which \bar{h} is closest to δ_v . The total uncertainty is calculated based on equation (18), showing that the total uncertainty in the best cases in $u_0 = 30, 40, 50,$ and 60 m s^{-1} is 3.22%, 3.11%, 3.02%, and 3.07%, respectively. Figure 13 shows the

Table 4. Uncertainties of elements and total uncertainty.

	u_0 (m s ⁻¹)	U_μ/μ (%)	U_{x_*}/x_* (%)	U_{t_*}/t_* (%)	$U_{v_{vol}}/v_{vol}$ (%)	$U_{r_{cal}}/r_{cal}$ (%)	$U_{\hat{\tau}}/\hat{\tau}$ (%)	U_τ/τ (%)	U_τ (Pa)
Group 1	20	2.23	0.202	0.019	1.65	0.0037 ^a	4.04 ^a	4.93 ^a	0.0834 ^a
	30	2.23	0.202	0.019	1.65	0.0037 ^a	3.57 ^a	4.56 ^a	0.151 ^a
	40	2.24	0.202	0.019	1.65	0.0037 ^a	5.73 ^a	6.39 ^a	0.262 ^a
Group 2	20	2.29	0.203	0.008	1.65	0.0024 ^a	3.66 ^a	4.66 ^a	0.0476 ^a
	30	2.25	0.203	0.008	1.65	0.0024	1.49	3.22	0.0582
	40	2.31	0.203	0.008	1.65	0.0024	1.11	3.11	0.0970
	50	2.34	0.203	0.008	1.65	0.0024	0.76	3.02	0.190
	60	2.33	0.203	0.008	1.65	0.0024	0.96	3.07	0.323
Group 3	30	2.29	0.202	0.008	1.65	0.0025	3.00	4.17	0.0877
	40	2.31	0.202	0.008	1.65	0.0024	1.96	3.50	0.118
	50	2.35	0.202	0.008	1.65	0.0024	1.83	3.45	0.181
	60	2.34	0.202	0.008	1.65	0.0025	2.35	3.75	0.268

^a Image uncertainty was estimated.

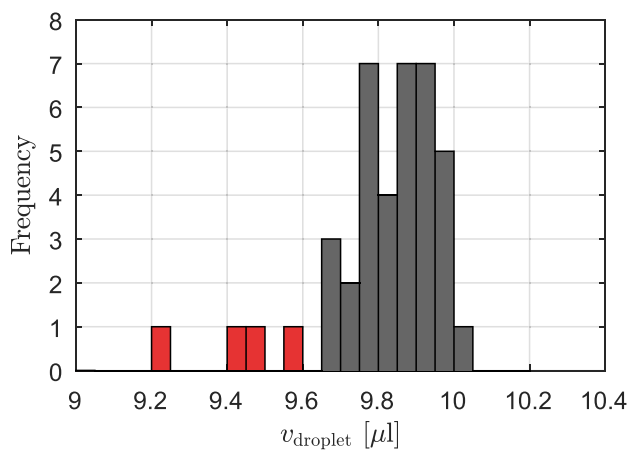


Figure 12. Histogram of oil droplet volume $v_{droplet}$. A total of 40 drops of oil were measured. Outliers are marked in red.

skin-friction values and their total uncertainties that satisfy $0.95\delta_v \leq \overline{h^+} < 1.05\delta_v$ —measurements when the average oil-film thickness is close to the viscous sublayer thickness. The selected GLOF measurement results show good agreement with those of the Clauser chart method and the von Kármán–Schoenherr equation. The uncertainty, however, does not cover the variations of the measured values. These variations may come from the other error sources that are not included in the uncertainty analysis.

The measurements that had the largest contribution to the total uncertainty were μ and v_{vol} , which can be improved by an accurate temperature/viscosity calibration and a better oil drop volume measurement, respectively. The temperature sensitivity of the oil viscosity is a dominant error source in oil-film interferometry measurements as well [3]. To reduce the uncertainty of $\hat{\tau}$, the optimum oil-film distribution, its shape, and the number of images should be considered [20].

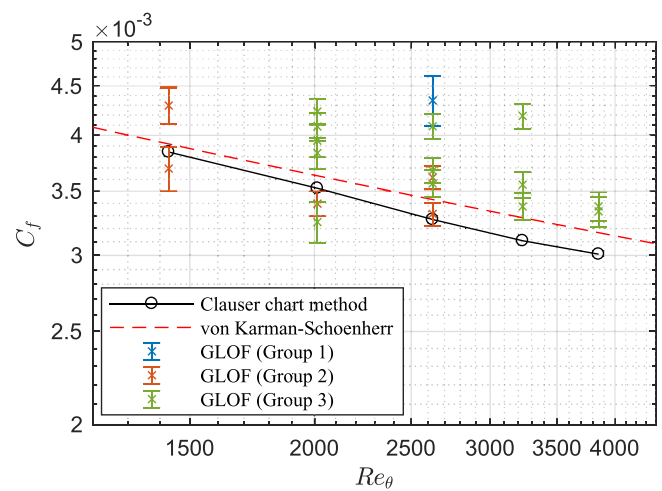


Figure 13. Skin-friction coefficient against momentum-thickness Reynolds number. The error bars indicate the total uncertainty.

6. Conclusions

In this study, the global luminescent oil-film method was tested on a flat plate model, and its uncertainty was analyzed. The overall process of obtaining the skin-friction field from luminescent oil-film images was explained, which includes the working principal, the image processing method based on LLS, the optical measurement settings, the calibration procedures, the numerical process, and the evaluation methods. The measurement errors related to each process were specified, and the resulting total uncertainty was obtained. The measured result was compared with a reference measurement determined from velocity profiles measured using a hot wire.

The results show that the GLOF skin-friction measurement matches well with that determined using the Clauser chart method when the oil-film thickness is close to the viscous sublayer thickness. When the oil film is thicker than the viscous

sublayer thickness, the surface becomes hydraulically rough due to the oil film, and the skin friction becomes larger. The criteria can be checked by the average oil-film thickness in the estimated wall units. It shows that the GLOF measurement is a standalone quantitative measurement technique.

The total uncertainty in the best cases was approximately 3%. The thinner oil-film height increases the uncertainty due to the image noise and the image processing, and reduces the coefficient of determination. For the measured variables studies, the largest uncertainties are due to the oil viscosity and calibration oil drop volume. Calibrating the oil as a function of temperature and measuring the temperature accurately help to reduce this error. Similarly, accurate measurements of the oil droplet volume and using lots of oil drops and averaging help reduce that uncertainty.

In practice, controlling proper oil heights in a complex flow is difficult. The oil is removed in an attached region, and the oil accumulates in a separated region. It is conceivable to supply to the region where the oil film is excluded from outside the region of interest and remove oil in regions where the oil is concentrated. When the oil flow is modified, the calculation region should be carefully set. Also, it is difficult to minimize uncertainty in all regions simultaneously. This could be partially addressed by using images from different time frames and/or different time intervals for different regions.

Acknowledgments

This work was partially supported by JSPS KAKENHI Grant No. 16H04582 and JST Presto Grant No. JPMJPR1678.

Appendix. Derivation of image error sensitivity coefficient

The uncertainty of $\hat{\tau}$ consists of the uncertainty of ratioed image $U_{\mathbf{r}_k}$. When $U_{\mathbf{r}_k}$ is assumed to be replaced by the representative value U_r , which means each image pixel error is not correlated to others, the uncertainty propagation equation is

$$U_{\hat{\tau}}^{\circ 2} = \sum_k \left\{ \left(\frac{\partial \hat{\tau}}{\partial \mathbf{r}_k} \right)^{\circ 2} U_{\mathbf{r}_k}^{\circ 2} \right\} \simeq U_r^2 \sum_k \left\{ \left(\frac{\partial \hat{\tau}}{\partial \mathbf{r}_k} \right)^{\circ 2} \mathbf{j} \right\} \equiv U_r^2 \mathbf{s}^{\circ 2}, \quad (\text{A.1})$$

where \mathbf{s} is the sensitivity coefficient vector, $^{\circ}$ is the Hadamard product, and \mathbf{j} is a vector of ones. The partial derivative of $\hat{\tau}$ with respect to \mathbf{r}_k is

$$\begin{aligned} \frac{\partial \hat{\tau}}{\partial \mathbf{r}_k} &= \frac{\partial \mathbf{C}^{-1} \mathbf{d}}{\partial \mathbf{r}_k} = \frac{\partial \mathbf{C}^{-1}}{\partial \mathbf{r}_k} \mathbf{d} + \mathbf{C}^{-1} \frac{\partial \mathbf{d}}{\partial \mathbf{r}_k} \\ &= -\mathbf{C}^{-1} \frac{\partial \mathbf{C}}{\partial \mathbf{r}_k} \mathbf{C}^{-1} \mathbf{d} + \mathbf{C}^{-1} \frac{\partial \mathbf{d}}{\partial \mathbf{r}_k} = -\mathbf{C}^{-1} \left(\frac{\partial \mathbf{C}}{\partial \mathbf{r}_k} \hat{\tau} - \frac{\partial \mathbf{d}}{\partial \mathbf{r}_k} \right), \end{aligned} \quad (\text{A.2})$$

where

$$\begin{aligned} \frac{\partial \mathbf{C}}{\partial \mathbf{r}_k} \hat{\tau} &= \frac{\partial (\mathbf{A}_k^T \mathbf{A}_k)}{\partial \mathbf{r}_k} \hat{\tau} \\ &= \left\{ \frac{\partial \mathbf{A}_k^T}{\partial \mathbf{r}_k} \mathbf{A}_k + \mathbf{A}_k^T \frac{\partial \mathbf{A}_k}{\partial \mathbf{r}_k} \right\} \hat{\tau} \\ &= \frac{1}{2} \text{diag} \left(\mathbf{M}_{\text{c2f}} \mathbf{r}_k \circ \left\{ \Delta_{\mathbf{x}}^T \Delta_{\mathbf{x}} \left(\mathbf{M}_{\text{c2f}} \mathbf{r}_k \circ \mathbf{M}_{\text{c2f}} \mathbf{r}_k \circ \hat{\tau} \right) \right\} \right) \mathbf{M}_{\text{c2f}} \\ &\quad + \frac{1}{2} \text{diag} \left(\mathbf{M}_{\text{c2f}} \mathbf{r}_k \circ \mathbf{M}_{\text{c2f}} \mathbf{r}_k \right) \Delta_{\mathbf{x}}^T \Delta_{\mathbf{x}} \text{diag} \left(\mathbf{M}_{\text{c2f}} \mathbf{r}_k \circ \hat{\tau} \right) \mathbf{M}_{\text{c2f}}, \end{aligned} \quad (\text{A.3})$$

$$\begin{aligned} \frac{\partial \mathbf{d}}{\partial \mathbf{r}_k} &= \frac{\partial (\mathbf{A}_k^T \mathbf{b}_k)}{\partial \mathbf{r}_k} = \frac{\partial \mathbf{A}_k^T}{\partial \mathbf{r}_k} \mathbf{b}_k + \mathbf{A}_k^T \frac{\partial \mathbf{b}_k}{\partial \mathbf{r}_k} \\ &= -\text{diag} \left(\mathbf{M}_{\text{c2f}} \mathbf{r}_k \circ \Delta_{\mathbf{x}}^T \Delta_{\mathbf{t}} \mathbf{M}_{\text{c2n}} \mathbf{r}_k \right) \mathbf{M}_{\text{c2f}} \\ &\quad - \frac{1}{2} \text{diag} \left(\mathbf{M}_{\text{c2f}} \mathbf{r}_k \circ \mathbf{M}_{\text{c2f}} \mathbf{r}_k \right) \Delta_{\mathbf{x}}^T \Delta_{\mathbf{t}} \mathbf{M}_{\text{c2n}}. \end{aligned} \quad (\text{A.4})$$

As a result,

$$\mathbf{s}^{\circ 2} = \frac{1}{4} \sum_k \left\{ (\mathbf{C}^{-1} \mathbf{G}_k)^{\circ 2} \mathbf{j} \right\}, \quad (\text{A.5})$$

where

$$\begin{aligned} \mathbf{G}_k &= \text{diag} \left(\mathbf{M}_{\text{c2f}} \mathbf{r}_k \circ \left\{ \Delta_{\mathbf{x}}^T \Delta_{\mathbf{x}} \left(\mathbf{M}_{\text{c2f}} \mathbf{r}_k \circ \mathbf{M}_{\text{c2f}} \mathbf{r}_k \circ \hat{\tau} \right) \right\} \right) \mathbf{M}_{\text{c2f}} \\ &\quad + \text{diag} \left(\mathbf{M}_{\text{c2f}} \mathbf{r}_k \circ \mathbf{M}_{\text{c2f}} \mathbf{r}_k \right) \Delta_{\mathbf{x}}^T \Delta_{\mathbf{x}} \text{diag} \left(\mathbf{M}_{\text{c2f}} \mathbf{r}_k \circ \hat{\tau} \right) \mathbf{M}_{\text{c2f}} \\ &\quad + 2 \text{diag} \left(\mathbf{M}_{\text{c2f}} \mathbf{r}_k \circ \Delta_{\mathbf{x}}^T \Delta_{\mathbf{t}} \mathbf{M}_{\text{c2n}} \mathbf{r}_k \right) \mathbf{M}_{\text{c2f}} \\ &\quad + \text{diag} \left(\mathbf{M}_{\text{c2f}} \mathbf{r}_k \circ \mathbf{M}_{\text{c2f}} \mathbf{r}_k \right) \Delta_{\mathbf{x}}^T \Delta_{\mathbf{t}} \mathbf{M}_{\text{c2n}}. \end{aligned} \quad (\text{A.6})$$

ORCID iDs

Taekjin Lee  <https://orcid.org/0000-0002-4606-2878>
 Taku Nonomura  <https://orcid.org/0000-0001-7739-7104>
 Jonathan W Naughton  <https://orcid.org/0000-0002-5903-8500>

References

- [1] Winter K G 1977 An outline of the techniques available for the measurement of skin friction in turbulent boundary layers *Prog. Aerosp. Sci.* **18** 1–57
- [2] Hanratty T J and Campbell J A 1983 Measurement of wall shear stress *Fluid Mechanics Measurements* 2nd edn, ed R Goldstein (Washington DC: Taylor and Francis) ch 9, pp 575–648
- [3] Naughton J W and Sheplak M 2002 Modern developments in shear-stress measurement *Prog. Aerosp. Sci.* **38** 515–70
- [4] Plesniak M and Peterson S 2004 Wall shear stress measurements for conventional applications and biomedical flows *24th AIAA Aerodynamic Measurement Technology and Ground Testing Conf.* p 2301
- [5] Reda D C, Wilder M C, Mehta R D and Zilliac G 1998 Measurement of continuous pressure and shear distributions using coating and imaging techniques *AIAA J.* **36** 895–9

- [6] Fonov S, Jones G, Crafton J, Fonov V and Goss L 2006 The development of optical techniques for the measurement of pressure and skin friction *Meas. Sci. Technol.* **17** 1261
- [7] Depardon S, Lasserre J J, Boueilh J C, Brizzi L E and Borée J 2005 Skin friction pattern analysis using near-wall PIV *Exp. Fluids* **39** 805–18
- [8] Chen L, Suzuki T, Nonomura T and Asai K 2019 Characterization of luminescent mini-tufts in quantitative flow visualization experiments: surface flow analysis and modelization *Exp. Therm. Fluid Sci.* **103** 406–17
- [9] Brown J L and Naughton J W 1999 The thin oil film equation *Technical Report* NASA, Washington, DC
- [10] Tanner L H and Blows L G 1976 A study of the motion of oil films on surfaces in air flow, with application to the measurement of skin friction *J. Phys. E: Sci. Instrum.* **9** 194
- [11] Monson D J, Mateer G G and Menter F R 1993 Boundary-layer transition and global skin friction measurement with an oil-fringe imaging technique *SAE Trans.* **1829–43**
- [12] Naughton J W and Brown J L 1996 Surface interferometric skin-friction measurement technique *Advanced Measurement and Ground Testing Conf.* p 2183
- [13] Zilliac G C 1996 Further developments of the fringe-imaging skin friction technique *Technical Report* NASA, Washington, DC
- [14] Garrison T J and Ackman M 1998 Development of a global interferometer skin-friction meter *AIAA J.* **36** 62–8
- [15] Liu T and Sullivan J 1998 Luminescent oil-film skin-friction meter *AIAA J.* **36** 1460–5
- [16] Liu T, Montefort J, Woodiga S, Merati P and Shen L 2008 Global luminescent oil-film skin-friction meter *AIAA J.* **46** 476–85
- [17] Mosharov V E, Orlov A A and Radchenko V N 2006 Application of correlation analysis in surface flow visualization with oil film *Proc. SPIE* vol 6262 Optical Methods of Flow Investigation p 62620B
- [18] Kurita M and Iijima H 2017 Hybrid oil film approach to measuring skin friction distribution *Meas. Sci. Technol.* **28** 055301
- [19] Husen N M, Liu T and Sullivan J P 2018 Luminescent oil film flow tagging skin friction meter applied to Faith hill *AIAA J.* **56** 3875–86
- [20] Lee T, Nonomura T, Asai K and Liu T 2018 Linear least-squares method for global luminescent oil film skin friction field analysis *Rev. Sci. Instrum.* **89** 065106
- [21] Husen N M, Liu T and Sullivan J P 2018 The ratioed image film thickness meter *Meas. Sci. Technol.* **29** 065301
- [22] Björck Å 1996 *Numerical Methods for Least Squares Problems* vol 51 (Philadelphia, PA: SIAM)
- [23] Bevington P R and Robinson K D 2003 *Data Reduction and Error Analysis for the Physical Sciences* 3rd edn (New York: McGraw-Hill) pp 39–110
- [24] Heller C A, Henry R A, McLaughlin B A and Bliss D E 1974 Fluorescence spectra and quantum yields. Quinine, Uranine, 9, 10-diphenylanthracene, and 9, 10Bis(phenylethynyl)anthracenes *J. Chem. Eng. Data* **19** 214–9
- [25] Von Kármán T 1931 Mechanical similitude and turbulence *Technical Report* National Advisory Committee on Aeronautics, Washington, DC
- [26] Ludwig H and Tillmann W 1950 Investigations of the wall-shearing stress in turbulent boundary layers *Technical Report* (Washington, DC: NASA)
- [27] Bradshaw P and Huang G P 1995 The law of the wall in turbulent flow *Proc. R. Soc. A* **451** 165–88
- [28] Clauser F H 1956 The turbulent boundary layer *Advances in Applied Mechanics* vol 4 (Amsterdam: Elsevier) pp 1–51
- [29] Wei T, Schmidt R and McMurtry P 2005 Comment on the Clauser chart method for determining the friction velocity *Exp. Fluids* **38** 695–9
- [30] Hopkins E J and Inouye M 1971 An evaluation of theories for predicting turbulent skin friction and heat transfer on flat plates at supersonic and hypersonic Mach numbers *AIAA J.* **9** 993–1003
- [31] Shin-Etsu Chemical Co., Ltd. 2005 *Silicone Fluid DM-FLUID Performance Test Results* (Tokyo: Shin-Etsu Chemical Co., Ltd.)
- [32] Ruedi J D, Nagib H, Österlund J and Monkewitz P A 2003 Evaluation of three techniques for wall-shear measurements in three-dimensional flows *Exp. Fluids* **35** 389–96
- [33] Bottini H, Kurita M, Iijima H and Fukagata K 2015 Effects of wall temperature on skin-friction measurements by oil-film interferometry *Meas. Sci. Technol.* **26** 105301
- [34] Lee T and Liu T 2018 Global luminescent oil film image based skin friction field estimator *Available online* (<https://github.com/technolojin/GLOFSFE>)
- [35] Horn B K P and Schunck B G 1981 Determining optical flow *Artif. Intell.* **17** 185–203
- [36] Naughton J W and Brown J L 1997 Uncertainty analysis for oil-film interferometry skin-friction measurement techniques *Proc. of the ASME Fluids Engineering Division Summer Meeting* (New York: American Society of Mechanical Engineers) p 3475
- [37] Hamamatsu Photonics K K 2017 *ORCA-Flash4.0 V3 Digital CMOS Camera C13440-20CU / C13440-20CU01 Instruction manual* (Japan: Hamamatsu, Shizuoka)
- [38] NF Corp. 2015 *Multifunction Generator WF1973 / WF1974 Instruction Manual (Basics)* (Japan: Yokohama)
- [39] Eppendorf A G 2013 *Biomaster 4830 Operating Manual* (Germany: Hamburg)